JOURNAL OF AIRCRAFT
Vol. 47, No. 6, November–December 2010

Nonlinear Modeling and Aeroelastic Analysis of an Adaptive Camber Wing

Guclu Seber* and Evren Sakarya†
Middle East Technical University, Ankara 06531, Turkey

DOI: 10.2514/1.C000312

Static aeroelastic analysis of an adaptive camber wing subjected to low-speed subsonic flow is presented. In finite element modeling follower forces, geometric nonlinearity, and contact definitions are included to accurately integrate a previously designed hingeless control surface into the wing. Camber variation is controlled at six spanwise stations using actuators for which actuation force magnitudes are determined iteratively using linearized influence coefficients. Flow solutions are obtained using a high-order panel method, and aeroelastic coupling is performed using the in-house code SAMOA. For morphed-wing configurations, induced drag is reduced by creating washout. By conducting static aeroelastic analysis actuation, force magnitudes are determined and favorable aerodynamic effects are identified. Results indicate that use of a nonlinear structural model is essential in capturing the stiffening behavior observed during application of spanwise variable camber.

I. Introduction

THE requirement to adapt to changing flight conditions has been essential since the early days of aviation. Use of systems such as high-lift devices and variable-sweep wings enable conventional aircraft to improve performance within their designated operational range. However, since aircraft are usually optimized for a limited number of discrete design points, the performance gains cannot be maximized within the full flight envelope [1,2]. Morphing technology provides the means for performance optimization for the complete flight envelope.

Although the definition of morphing still varies among the technical community, it is generally accepted that morphing corresponds to a state change that targets efficiency and adaptability. A more recent definition declares morphing as "real-time adaptation to enable multipoint optimized performance" [3].

During morphing, air vehicles exhibit local or global transformations using smart and/or conventional actuators [3,4]. In some of the most recent studies [5–17] the use of unconventional designs featuring mechanisms or compliant structures that employ composite or elastomer-type materials appears to be the most common point. To define morphing and to quantify the benefits a formal assessment process [18] may be adopted.

Morphing aircraft can accommodate large changes in wing planform area, sweep angle, and span [8,9] to have multiple roles and fulfill conflicting performance requirements. Another form of morphing involves wings with variable camber [1,2,4–7,10,14,17], where smooth aerodynamic surfaces are created to accommodate laminar flows [2,10]. By applying spanwise camber variations, aerodynamic loads can be redistributed adaptively during the flight to balance the weight decrease due to fuel burn, minimize drag, and reduce wing root bending moments [1,2]. The potential increase in lift-to-drag ratio varies between 3 to 10% for a typical transport-type aircraft during cruise [1].

In most applications of wings with variable camber, conventional structures are replaced or modified to increase the flexibility in a controlled manner. For instance, the belt-rib [5] approach uses multiple spokes that permit camber variations to replace the traditional ribs. The compliant trailing-edge flap developed by Flexsys, Inc., [10] uses elasticity to recontour the upper and lower skins. Analysis and flight tests have shown that this lightweight and low-power design can maintain long laminar runs and low drag, even with significant camber variations.

As an alternative to compliant structures, rotating (or deformable) ribs of either single-piece [4,6,7,17] or multiple segments [1] combined with mechanisms are also used. When ribs are rotated, skins flex and sliding is facilitated by the presence of open trailing edge. These features reduce structural stresses and actuation force magnitudes.

In this study, the nonlinear finite element modeling and analysis are done using MSC PATRAN [19] and MD NASTRAN [20], respectively. A code is developed to perform static aeroelastic analyses of an adaptive camber wing (ACW). Steady-state aerodynamic loads are calculated using the high-order panel code PAN AIR [21]. For an accurate representation of the fluid–structure interface, local shape functions are used to interpolate displacements and pressures. By using an iterative process, which employs linearized influence coefficients, actuation force magnitudes are calculated for morphing wings subject to spanwise camber variation.

II. Concept Description and the Structural Model

Figure 1 shows the ACW with the full-span hingeless control surface (HCS) and NACA 4412 airfoil section. A rectangular planform with 0.5 m chord and 1.5 m semispan is chosen to simplify the models and better interpret the results. The HCS design is based on the concept by Seber et al. [17] that exploits controlled structural flexibility to accommodate camber variations. Some unconventional elements such as a semi-open trailing edge, i.e., only sliding in chordwise direction is permitted, and cutout ribs are featured. However, no major structural modifications are required at the traditional semimonocoque torque box, and the ACW is considered to be made out of standard aluminum 2024-T3 alloy.

To apply camber variations, servo actuators initiate sliding at the guide-slide assemblies (GSAs) via push-rods that are connected to the cutout ribs (see Fig. 2). Sliding flexes the upper and lower skins between the torque box and the cutout ribs. GSAs maintain integrity by preventing the separation of lower and upper skins at the trailing edge, and they are basically prismatic joints. The two main components (namely, the cutout ribs and the tracks) are rigidly connected to upper and lower skins, respectively, but not to each other. The current model features GSAs that are aligned with the main ribs that are 28 cm apart.

Received 18 February 2010; revision received 12 June 2010; accepted for publication 15 June 2010.

*Assistant Professor, Department of Aerospace Engineering; currently Research Scientist, Virginia Polytechnic Institute and State University, Blacksburg, VA 24061-0203; gseber@vt.edu.

†Research Assistant, Department of Aerospace Engineering; esakarya@ae.metu.edu.tr.

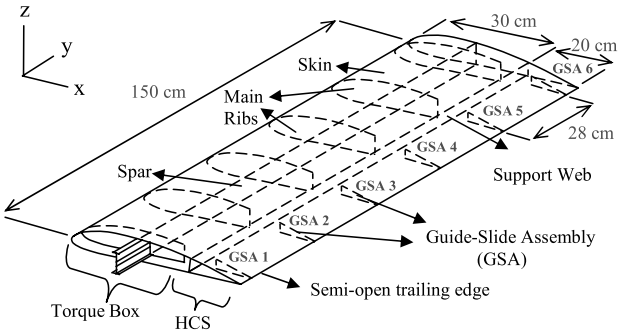

Fig. 1 Components of the ACW with the full-span HCS.

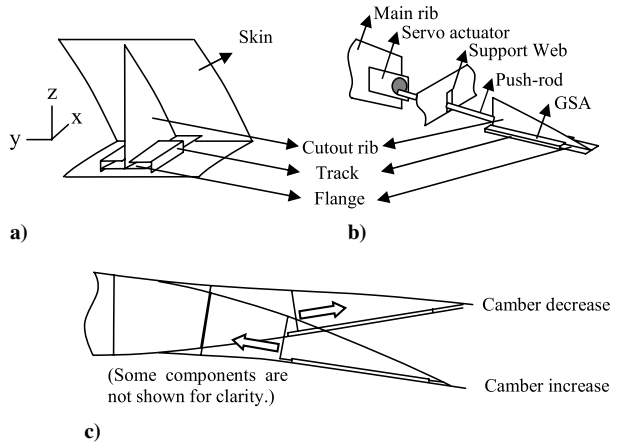

Fig. 2 Detailed views of a) GSA, b) actuation system, and c) camber variations.

Cutout ribs provide the required structural flexibility during camber changes; however, they also introduce a structural weakness at the skins. To reinforce and stabilize the skins, a support web is introduced. The support web is not rigidly connected to the skins, but via hinge joints to permit rotation about a spanwise axis. It is also oriented in a slanted fashion with respect to vertical, so sliding is not constrained during camber variations (see [17]).

The use of cutout ribs and semi-open trailing edge decouples the in-plane stretching of upper and lower skins during flexing. The actuation system controls the flexibility introduced by unconventional features. The push-rods act as axial members that transmit loads to the servo actuators located at the main ribs. It is assumed that the push-rods and the servo actuators are robust enough to resist the loads to which they are subjected.

Figures 3a and 3b show the finite element model of the ACW, which is created using MSC PATRAN [19], and the components of the actuation system, respectively. Fixed-end boundary conditions are applied at the root spar extension. Different components are represented by 2716 finite element nodes, 2568 shell-type four-node quadrilateral (CQUAD4) and three-node triangular (CTRIA3) finite elements, 202 Euler–Bernoulli beam-type two-node (CBEAM) finite elements, and 12 multipoint constraints (MPCs). Table 1 presents the structural properties of the model.

The implicit nonlinear solver of MD NASTRAN [20] is used for static analysis. In the formulation, geometric nonlinearity, stress-stiffening, follower forces, and contact phenomena are included, and linear elastic material behavior is assumed. The equations for a nonlinear system is expressed as

$$[K^T]\{\Delta u\} = \{P\} - \{R\} = \{r\} \tag{1}$$

where $[K^T]$ is the tangent stiffness matrix; $\{\Delta u\}$ is the incremental displacement vector; $\{P\}$ and $\{R\}$ are the external and elastic force vectors, respectively; and $\{r\}$ is the residual.

During mesh generation conforming mesh seeds are applied along the edges to create coincident nodes. Duplicate nodes are then eliminated to create rigid connections except for the semi-open trailing edge. Double-sided contact elements are defined at the cutout ribs, tracks and lower skin surfaces to model sliding. MPCs that connect the edge nodes of the support web to upper and lower skins represent the hinge-type joints. The servo actuators are modeled as six pairs of equal-and-opposite forces acting along the same line of action at all times.

As shown in Fig. 4, trailing-edge deflections, which are designated by δ, are applied at each GSA to create camber variations. Since ACW cross sections translate and rotate as deformations occur under aerodynamic loads, trailing-edge deflections are defined relative to main ribs that remain mostly rigid. Figure 4 shows the planar unit vectors $\mathbf{v_0}$, $\mathbf{v_1}$, and $\mathbf{v_2}$ and angles θ_1, θ_2, and θ that are defined to exclude the effects of deformations from the trailing-edge deflections. The unit vectors are along |AO|, |AB| and |AB′|, which correspond to the main rib reference line, chord lines before and after the trailing-edge deflection is applied, respectively. Nodes O, A, and B, which are used to define the aforementioned lines, are located at the rear edge of the main rib, leading edge, and trailing edge, respectively. At each GSA, δ is given by

$$\delta = |\mathrm{AB}'| \sin(\theta_2 - \theta_1) = |\mathrm{AB}'| \sin(\theta) \tag{2}$$

Angles θ_1 and θ_2 in Eq. (2) are defined in terms of unit vectors $\mathbf{v_0}$, $\mathbf{v_1}$, $\mathbf{v_2}$ and $\mathbf{j}$ as follows:

$$\theta_i = \sin^{-1}(\mathbf{v_0} \times \mathbf{v_i})\mathrm{sign}[(\mathbf{v_0} \times \mathbf{v_i}) \cdot \mathbf{j}] \tag{3}$$

III. Calculation of Actuation Force Magnitudes

One of the main objectives of this study is to develop a procedure to determinate the actuation force magnitudes corresponding to a specific spanwise camber variation. With this information, the requirements on actuators could be determined, and future tradeoff studies could be conducted. To achieve this objective, flexibility and stiffness influence coefficients are used in a linearized manner. For a linear system, where principle of superposition is valid, the relations between n generalized coordinates q_i and forces Q_i are given by

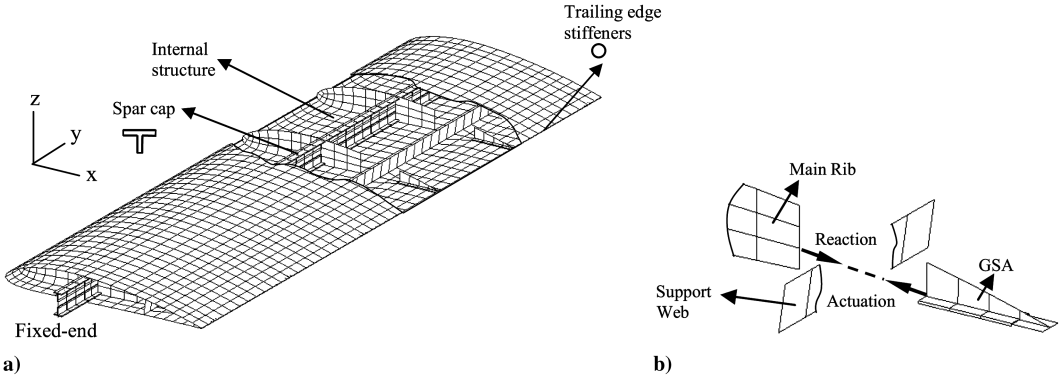

Fig. 3 Illustrations of a) ACW finite element model and b) components of the actuation system.

Table 1 Properties of the ACW finite element model

Parameter	Value
Skin thickness	0.635 mm
Spar web thickness	1.6 mm
T-spar cap thickness	1.6 mm
T-spar cap height	19.05 mm
T-spar cap width	31.75 mm
Radii of the TE stiffeners	1.5 mm
Support web thickness	0.635 mm
Main rib thickness	0.635 mm
Cutout-rib thickness	0.635 mm
Track thickness	0.635 mm
Young's modulus	73.1 GPa
Poisson's ratio	0.33

$$q_i = \sum_{j=1}^{n} C_{ij} Q_j \tag{4}$$

$$Q_i = \sum_{j=1}^{n} S_{ij} q_j \tag{5}$$

where C_{ij} and S_{ij} are the flexibility and stiffness influence coefficients, respectively. By consecutively applying a single nonzero actuation and reaction force pair at each GSA, C_{ij} are calculated from the results of the finite element analyses as

$$C_{ij} = \delta_j^i / F_i \tag{6}$$

where i and j indices refer to GSAs that are numbered from 1 to 6, starting with the one closest to the wing root; δ_j^i is the trailing-edge deflection at the jth GSA due to the actuation force of magnitude F_i applied at the ith GSA; and δ_j^i and F_i are considered positive, if section camber increases.

By collecting the flexibility influence coefficients, the flexibility matrix $[C]$ is created and inverted to obtain the stiffness matrix $[S]$. In an iterative process, the corrective actuation force vector $\{\Delta F\}_n$ is obtained from

$$[C]^{-1}\{\Delta\delta\}_n = [S]\{\Delta\delta\}_n = \{\Delta F\}_n \tag{7}$$

where $\{\Delta\delta\}_n$ is the deflection error vector at iteration step n, which is obtained by taking the difference between the target trailing-edge deflections and those obtained from the finite element solution: i.e., $\{\Delta\delta\}_n = \{\delta\}^{\text{target}} - \{\delta\}_n^{\text{FE}}$ (FE denotes finite element solution). For the next iteration step the finite element analysis is repeated using the updated force vector given by

$$\{F\}_{n+1} = \{F\}_n + \{\Delta F\}_n \tag{8}$$

The above steps are repeated until the elements of $\{\Delta\delta\}_n$ are within the selected 0.5% error tolerance. In this process, the flexibility matrix $[C]$ is either determined by considering the undeformed state of the ACW, or by applying actuation force perturbations around an estimated equilibrium point. The perturbations are introduced by rewriting Eq. (6) to define the coefficients of the tangent flexibility matrix $C_{ij}^T = \nabla\delta_j^i / \nabla F_i$, where ∇ indicates the perturbations. The preliminary numerical tests conducted during the development stages of this process have shown that the former technique is applicable to problems in which aerodynamic loads are not present and nonlinearities are weak. The latter technique is more robust and efficient, especially during static aeroelastic analysis, since it represents the nonlinearities of the current state more accurately.

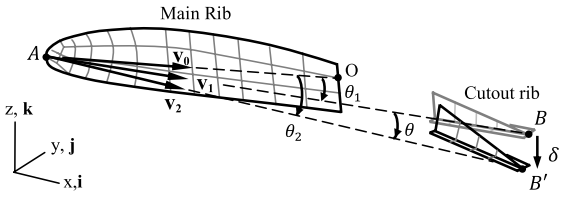

Fig. 4 Calculation of the trailing-edge deflection δ in the deformed state.

IV. Aerodynamic Modeling

PAN AIR [21] code by Boeing is employed to study the low-speed subsonic flow around the ACW. PAN AIR employs a higher-order panel method based on the solution of the linearized potential-flow problem for arbitrary 3-D configurations.

In panel method solutions, the wake location and shape must be prescribed as part of the geometry. In this study, a traditional approach is used for its simplicity. The edges of the wake panels are projected from the trailing edge straight downstream parallel to the far-field flow. Figure 5 shows the panels and the corresponding wake geometry. Half-sine and cosine-type distributions are used to create a network of 20 chordwise and 10 spanwise panels on the wing upper and lower surfaces, and the wake is extended downstream to 10 chord lengths.

In this study, the aerodynamic analyses are conducted by considering flow symmetry at the wing root with respect to the x-z plane. Compressibility corrections are made using Prandtl–Glauert relations. Within the assumption of attached flow, small-angle-of-attack values and camber variations are considered. Furthermore, it is assumed that the semi-open trailing edge and the wing tip are aerodynamically sealed using elastomer-type materials similar to those used in [9,10]. In future studies, the impact of using such materials will be investigated further.

V. Coupling of Structural and Aerodynamic Models

In literature, several studies focus on the aeroelastic behavior of variable-camber wings [5–8,11,22,23]. To carry out the same task, a code named SAMOA (Static Aeroelasticity of Morphing Aircraft) is developed in Python programming language.[‡] SAMOA couples structural and aerodynamic models and adjusts the actuation force magnitudes iteratively until the target spanwise camber variation is obtained. Figure 6 shows the flowchart of SAMOA.

Before the aeroelastic analysis, the flow properties and the target spanwise camber variation are assigned. Structural and aerodynamic models are also created. Since the solution meshes of the models are nonconforming at the fluid–structure interface, i.e., ACW outer surface, two mapping operations are performed. Vertices of aerodynamic panels are located within the quadrilateral finite elements, and finite element nodes are likewise located within the aerodynamic panels. For consistency, displacement and pressure values are calculated within the elements and panels, respectively, using the interpolation function:

$$\phi(\xi, \eta) = c_1 + c_2\xi + c_3\xi\eta + c_4\eta \tag{9}$$

where $\phi(\xi, \eta)$ refers to the interpolated displacement or pressure value, ξ and η are the natural coordinates of the element or the panel, and c_i are the coefficients that are in terms of the values at the nodes or the vertices.

To improve convergence time, aeroelastic analyses start from an initial estimate of the actuation forces. To get this estimate, the morphed ACW considered rigid, and the effect of deformations under the aerodynamic loads are ignored. During the analysis, pressure loads are calculated from the aerodynamic solution and are applied to the structural model. Since deformations reshape the ACW outer surface, the aerodynamic model is updated and pressure loads are recalculated at each step. By keeping the actuation force magnitudes constant, these steps are repeated until the deformations and the aerodynamic coefficients converge. If the calculated spanwise camber variation does not match the target within tolerance, the corrective actuation force vector $\{\Delta F\}_n$ is calculated as described in Sec. III.

[‡]Data available online at http://www.python.org/ [retrieved 10 February 2010].

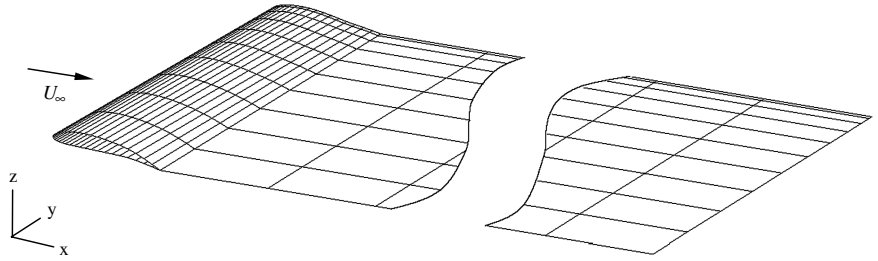

Fig. 5 Panels and the wake of the aerodynamic model.

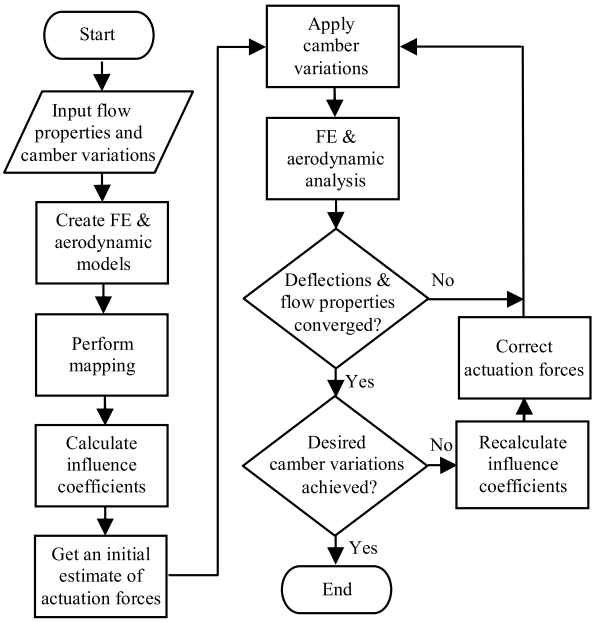

Fig. 6 Flowchart of SAMOA (FE denotes finite element).

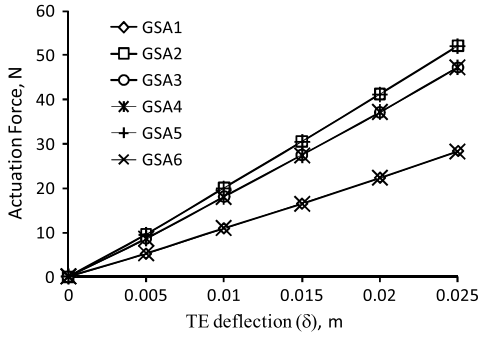

Fig. 7 Actuation force vs trailing-edge (TE) deflection behavior for uniform camber increase.

VI. Results

A. Structural Analysis of the ACW

To study the nonlinear structural effects, three case studies are conducted excluding the aerodynamic loads. In the first case study, a spanwise uniform camber increase is considered. Figure 7 shows that the actuation force magnitudes increase almost linearly with increasing δ values. Because of structural symmetry, the curves that are associated to GSAs 1, 2, and 3 are identical to those of 6, 5 and 4, respectively. Corresponding to a particular δ value, the actuation force magnitudes are the smallest at the most inboard and outboard GSAs: i.e., 1 and 6. At GSAs 2 to 5, actuation force magnitudes are about twice as much as those calculated at GSAs 1 and 6.

In the second and third case studies, spanwise variable trailing-edge deflections are applied. This way, camber variations are created that result in elliptical and linear washouts. These trailing-edge deflections are defined by

$$\delta(y) = \delta_{\text{tip}}[1 - \sqrt{1 - (y/b)^2}] \tag{10}$$

$$\delta(y) = \delta_{\text{tip}}(y/b) \tag{11}$$

where y is the span coordinate, b is the half wing span, and δ_{tip} is the trailing-edge deflection at the wing tip. In this papers context, washout refers to the combination of geometric and aerodynamic twist due to trailing-edge deflections, which results in a smaller effective angle of attack at the outboard wing sections. To create washout, negative δ_{tip} values are used in Eqs. (10) and (11).

The motivation behind creating washout may be explained by referring to work by Phillips [24], who has considered the effect of washout on the low Mach number performance of finite wings. By studying the aspects of linear and elliptical washout distributions, Phillips has shown that for wings of arbitrary planform, the induced drag may be minimized. This can be done if the product of the local chord length and the local angle of attack varies elliptically with the span coordinate. Therefore, the effects of adaptively creating elliptical and linear washouts are also studied in this paper.

Figures 8 and 9 show the actuation force magnitudes as a function of δ for elliptical and linear washout distributions, respectively. Plots indicate that the actuator force magnitudes increase nonlinearly with δ, especially for the elliptical washout distribution. Further examination of the results has shown that this behavior is attributed to in-plane deformations of the skins along the spanwise direction. These

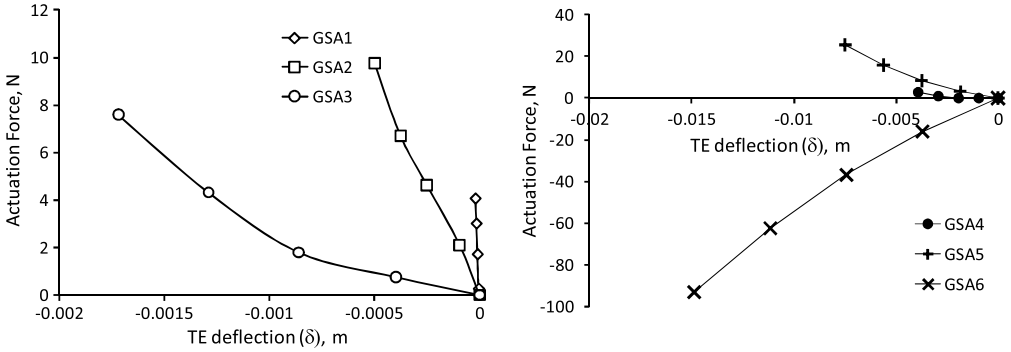

Fig. 8 Actuation force vs TE deflection behavior for elliptical washout.

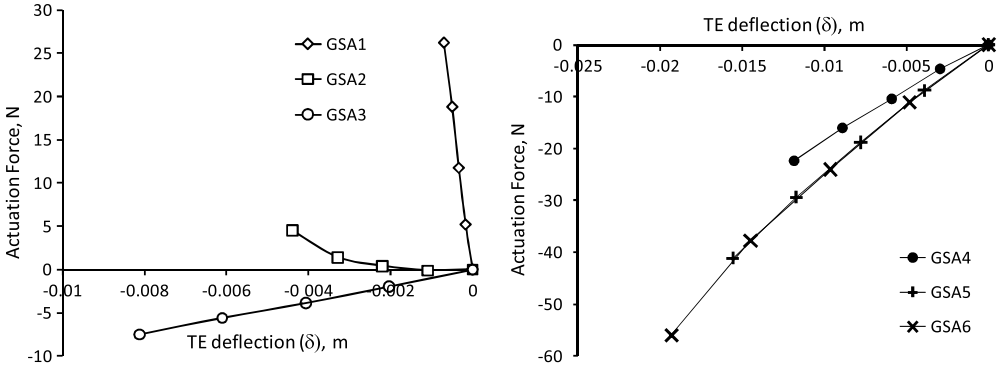

Fig. 9 Actuation force vs TE deflection behavior for linear washout.

deformations are created due to coupling effects associated with geometric nonlinearity and are several orders of magnitude smaller than the out-of-plane deformations. However, since the in-plane stiffness of the skins is considerably larger than the out-of plane stiffness, the nonlinear stress-stiffening behavior becomes quite strong during application of washout.

Figure 8 also shows that to create elliptical washout, a large actuation force of negative value is required at GSA 6. This large force must be counteracted by positive-valued actuation forces of relatively lower magnitudes at the other GSAs. As seen in Fig. 9 to create linear washout, negative-valued actuation forces are required at GSAs 3 to 6, which are counteracted by positive values actuation forces at GSAs 1 and 2. When results in Figs. 8 and 9 are compared, it is seen that the actuation force at GSA 6 is about 40 to 50% lower in magnitude for linear washout as compared to elliptical washout for the same δ_{tip} value.

B. Validation of SAMOA

To validate SAMOA, two test cases are considered using a simplified aeroelastic model that is derived from the original ACW finite element model. By using an MPC and a grounded torsional spring at the root spar extension, the model is constrained to rotate about an axis that runs along the spar. This configuration resembles a typical section model for which the twist θ about the elastic axis and the lift coefficient C_L may be determined using the analytical solution given by

$$\theta = \frac{qS[e(C_{L0} + C_{L\alpha}\alpha) + cC_{M0}]}{K_\theta - eqSC_{L\alpha}} \tag{12}$$

$$C_L = C_{L0} + C_{L\alpha}(\alpha + \theta) \tag{13}$$

where α is the flow angle of attack, q is the dynamic pressure, S and c are the wing area and chord length, respectively, e is the distance between the aerodynamic center and the elastic axis, C_{L0} is the lift coefficient at zero angle of attack, $C_{L\alpha}$ is the wing lift curve slope, C_{M0} is the moment coefficient with respect to the aerodynamic center, and K_θ is the torsional spring constant. Table 2 shows the parameters associated to test cases 1 and 2.

The results of SAMOA are compared to the analytical solution obtained from Eqs. (12) and (13) in Fig. 10. In case 1, the pitch-down effect of the increased wing camber dominates the moment due to lift. Therefore, both θ and C_L decrease with increasing flow speed. In case 2, the pitch-up moment due to lift is more dominant than the pitch-down moment due to camber, so both θ and C_L increase with increasing flow speed. At 22.5 m/s flow speed, which is close to the divergence speed of 25.3 m/s as predicted from Eq. (12), solutions show about 10% difference; but overall very good agreement exists. It is thought that since the aerodynamic data used in Eqs. (12) and (13) are based on fixed average values, the approximate nature of the parameters used in the analytical solution becomes more significant near the divergence speed and so does the discrepancy in results.

C. Aerodynamic and Static Aeroelastic Analysis of the ACW

To demonstrate the benefits of adaptive camber, analyses are conducted for two wing configurations that are referred to as wings A and B. Wing A operates at $C_L = 0.4$ and it accommodates washout. wing B features a uniform camber increase of $\delta = 0.01$ cm for an increased C_L of 0.6 onto which washout may further be imposed. Figure 11 presents the results of the aerodynamic analyses conducted by adjusting the flow angle of attack to maintain the designated C_L values. The curves show the effect of δ_{tip} on the induced-drag penalty, which is defined as the percent increase as compared to the induced-drag coefficient C_{Di} of an elliptical planform wing with the same C_L. For wing A, the minimum C_{Di} values are calculated at δ_{tip} values of -0.012 and -0.009 m with elliptical and linear washouts, respectively (see Fig. 11). For wing B these values are -0.016 and -0.01 m. Results show that the induced-drag penalty is reduced by 2.5 and 2.75 % for wings A and B, respectively. For both wings, the reduction in penalty with elliptical washout is only 0.1% better than the case with linear washout. The application of washout also reduces the root bending moments. For wing A, 4.5 and 5.1% reductions are observed at the minimum-drag conditions with elliptical and linear washouts, respectively. For wing B, these values are calculated as 3.9 and 3.8%.

The static aeroelastic analyses have been conducted at the minimum-drag conditions with a flow speed of 34 m/s at sea level. In Fig. 12, wing cross-sectional views are shown in which spanwise washout and dominantly bending-type deformations are present. Since deformations are relatively small in the torque box, i.e., about 4 to 5 mm, the structural model may be considered to be stiff, and the presence of the HCS does not create a particular structural weakness.

Figure 13 shows the stepped convergence behavior of C_L. Each step corresponds to analysis with a fixed magnitude actuation force set, which remains unchanged until convergence. Table 3 presents the aerodynamic results obtained. Compared to the rigid case, C_L values are larger than the designated 0.4 and 0.6 values, whereas the induced-drag penalties are, in fact, slightly lower. As the main ribs experience small in-plane deformations, the relative positions of the nodes used in δ calculations change. Camber bending also occurs at the HCS, as shown in Fig. 14. The combination of these effects leads to an overall increase in spanwise lift distributions, as shown in Fig. 15.

Table 2 SAMOA validation study parameters

Parameter	Value	
	Case 1	Case 2
α	4°	3.5°
δ	0.01 m	−0.01 m
C_{M0}	−0.1413	−0.0573
C_{L0}	0.5665	0.1367
e	0.0735 m	
c	0.5 m	
ρ	1.225 kg/m^3	
$C_{L\alpha}$	4.5714 1/rad	
K_θ	100 N · m/rad	
S	0.75 m^2	

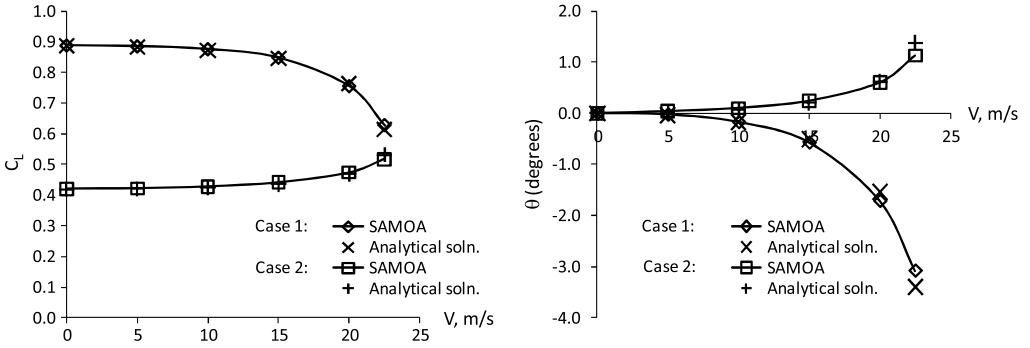

Fig. 10 Results of the validation study: SAMOA vs the analytical solution obtained from Eqs. (12) and (13).

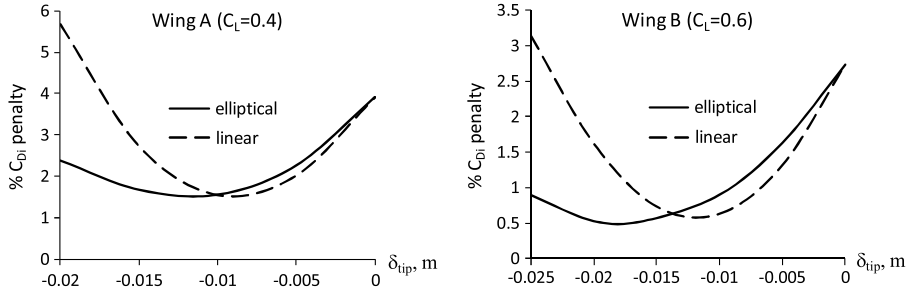

Fig. 11 Variation of % C_{Di} penalty with linear and elliptical washout.

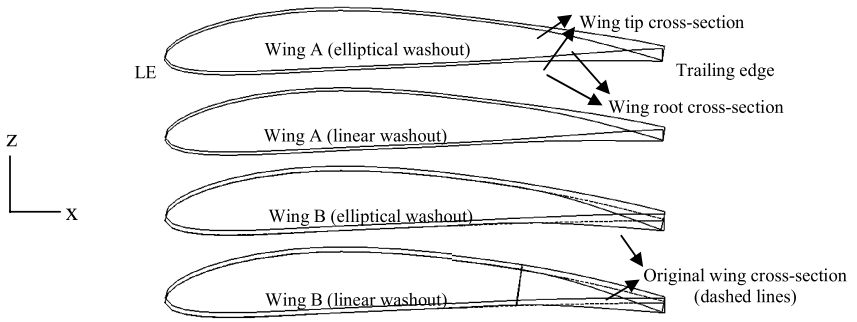

Fig. 12 Wing cross-sectional views showing aeroelastic deformations and washout.

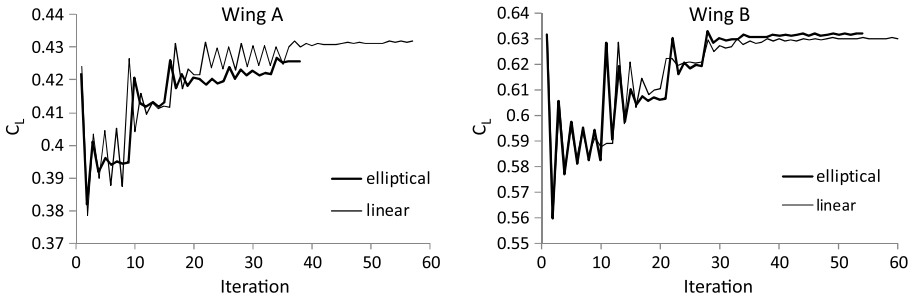

Fig. 13 Convergence of C_L at the minimum induced-drag conditions.

Table 3 C_L, C_{Di}, and $\%C_{Di}$ penalties as obtained from static aeroelastic analyses

	Elliptical washout			Linear washout		
	C_L	C_{Di}	$\%C_{Di}$ penalty	C_L	C_{Di}	$\%C_{Di}$ penalty
Wing A	0.4255	0.00971	1.08	0.4318	0.00998	0.91
Wing B	0.6319	0.02128	0.44	0.6302	0.02118	0.53

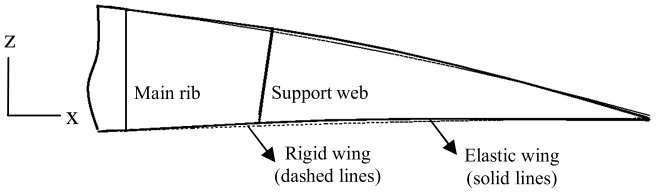

Fig. 14 Camber bending at wing A root due to aerodynamic loads and actuation forces.

For comparison purposes, curves corresponding to wings with no washout are also presented here.

Figure 16 illustrates the change in actuation force magnitudes in the presence of aerodynamic loads. For wing A with elliptical washout, the actuation force magnitudes at GSAs 1 to 5 increase significantly to overcome the aerodynamic loads that tend to decrease camber. However, the aerodynamic loads have a favorable effect at GSA 6 that lead to a 19.1% reduction. With linear washout, actuation force magnitudes at GSAs 1 to 4 increase to maintain the camber distribution of wing A. Furthermore, aerodynamic loads are more favorable than the elliptical washout case at GSAs 5 and 6, giving reductions of 76 and 44.7 %, respectively. For wing B, an increase at GSAs 1 to 5 and a decrease at GSA 6 are observed with both elliptical and linear washouts. The decrease at GSA 6 is 19.7%

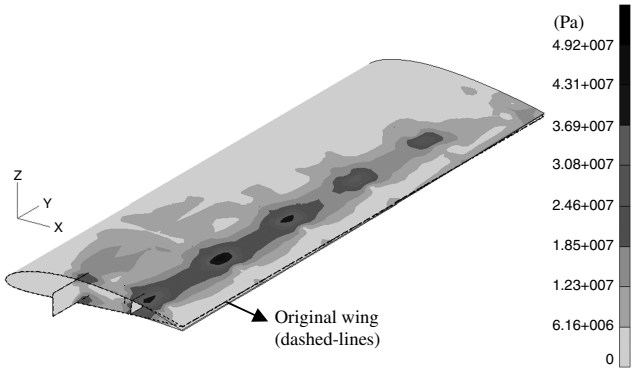

Fig. 17 Equivalent Cauchy stress contours for wing B with elliptical washout ($\sigma_{max} = 49.2$ MPa).

with elliptical washout, whereas with linear washout the actuation force magnitude nearly becomes zero. In all the cases considered, actuation force at GSA 2 has the largest magnitude in the presence of aerodynamic loads.

Figure 17 shows the stress contour plot of wing B with elliptical washout. A region of high stress exists on the flexed skins between the support web and the GSAs. A peak stress of 42.9 MPa is located at

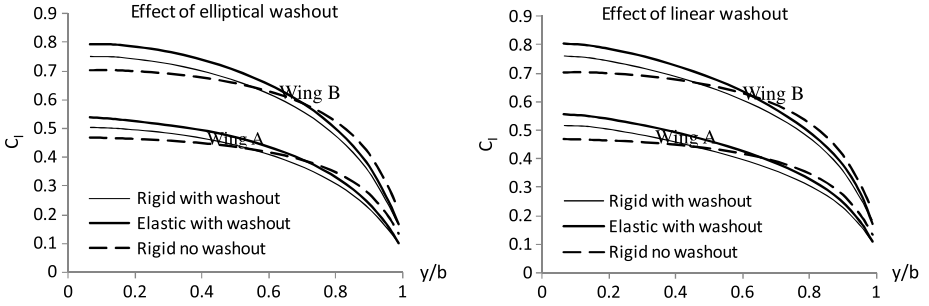

Fig. 15 Effect of washout and elasticity on the spanwise lift distribution.

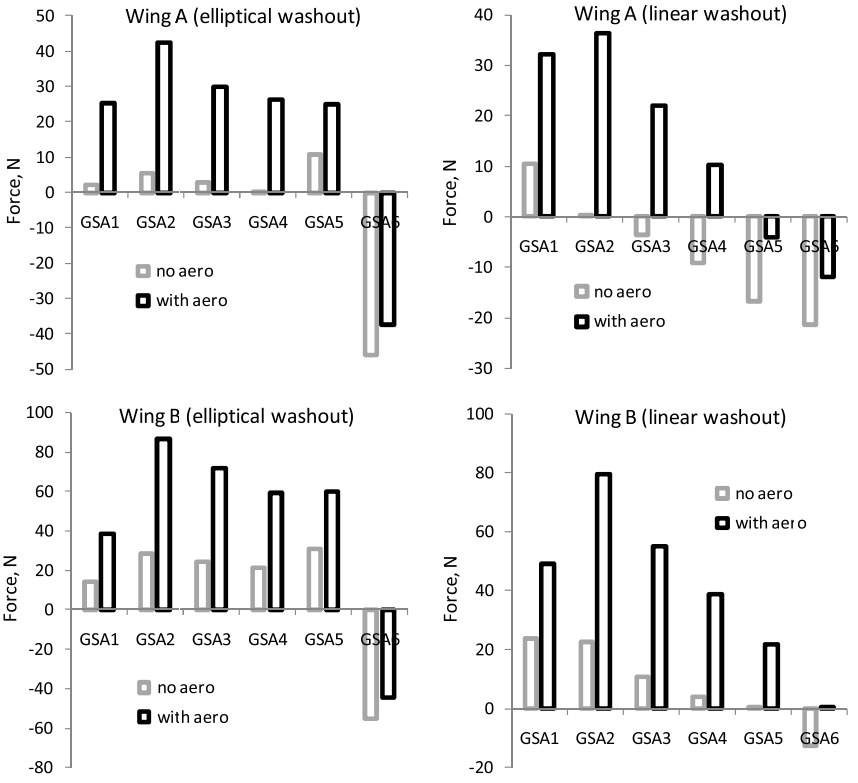

Fig. 16 Comparison of actuation force magnitudes with and without aerodynamic loads.

the upper skin just forward of GSA 2. The high stress values in this region gradually decrease toward the wing tip while exhibiting some smaller-valued local peaks. Since the peak stress value is much lower than the yield limit of aluminum 2024-T3 alloy, linear elastic material assumption remains valid for static loading. For other cases, the peak stress values are much lower, and therefore stress contour plots are not presented.

VII. Conclusions

The HCS concept previously developed has been successfully integrated with a traditional torque box, and the benefits of adaptive camber are demonstrated. Static aeroelastic analyses have been conducted for two morphed ACW configurations: namely, wings A and B, which are designated to operate at $C_L = 0.4$ and 0.6, respectively. During the analysis, actuation force magnitudes are calculated iteratively using linearized influence coefficients to obtain the target spanwise camber variation. Results indicate that with both elliptical and linear washouts, which are created by spanwise camber variations, it is possible to obtain reductions in root bending moments and induced drag. In accordance with the scope of this study, the aerodynamic benefits discussed in this paper are limited by the predictions of the linearized potential-flow theory. However, it is considered that a computational-fluid-dynamics-based aerodynamic model could better reveal the true aerodynamic benefits over a traditional control surface in the presence of viscous effects.

Structural stresses during camber variations are determined to be well under the material yield limit for static loading. Thus, the initial assumption of linear elastic behavior remains valid. When creating washout, the nonlinear coupling effects induce in-plane deformations and the resulting stress-stiffening behavior significantly increases the actuation force magnitudes. Use of a fully nonlinear structural model is essential for capturing these effects.

Static aeroelastic analyses indicate that at the majority of the GSAs, actuation force magnitudes increase to overcome the aerodynamic loads and maintain the section camber. At the most outboard GSAs, where washout is the largest, aerodynamic loads act favorably and reduce the actuation forces magnitudes.

The ACW under investigation offers some aerodynamic and structural benefits that show the potential of morphing technology. However, unique challenges also exist for this concept mainly due to nonlinear effects. It is considered that these challenges may be addressed in future studies using optimization techniques and advanced materials. With such studies, nonlinear structural effects may also be reduced and accurate linearized models could be created for use in free-vibration and flutter analyses. It is believed that, in turn, the benefits of this concept may further be assessed within a realistic operational context.

Acknowledgments

This research was supported by Turkish Scientific and Technological Research Council through the project TUBITAK/107M103, Aeroservoelastic Analysis of the Effects of Camber and Twist on Tactical Unmanned Aerial Vehicle Mission-Adaptive Wings. The authors gratefully acknowledge the support given.

References

[1] Monner, H. S., "Realization of an Optimized Wing Camber by Using Formvariable Flap Structures," *Aerospace Science and Technology*, Vol. 5, 2001, pp. 445–455. doi:10.1016/S1270-9638(01)01118-X

[2] Stanewsky, E., "Aerodynamic Benefits of Adaptive Wing Technology," *Aerospace Science and Technology*, Vol. 4, No. 7, 2000, pp. 439–452. doi:10.1016/S1270-9638(00)01069-5

[3] McGowan, A. R., Vicroy, D. D., Busan, R. C., and Hahn, A. S., "Perspectives on Highly Adaptive or Morphing Aircraft," *NATO-RTO Applied Vehicle Technology Panel (AVT) Symposium*, Evora, Portugal, 20–24 April 2009.

[4] Cavagna, L., Ricci, S., and Riccobene, L., "Application of Adaptive Camber Mechanism to Morphing Wings," *NATO-RTO Applied Vehicle Technology Panel (AVT) Symposium*, Evora, Portugal, 20–24 April 2009.

[5] Campanile, L. F., and Anders, S., "Aerodynamic and Aeroelastic Amplification in Adaptive Belt-Rib Airfoils," *Aerospace Science and Technology*, Vol. 9, No. 1, 2005, pp. 55–63. doi:10.1016/j.ast.2004.07.007

[6] Ricci, S., Scotti, A., and Terraneo, M., "Design, Manufacturing and Preliminary Test Results of an Adaptive Wing Camber Model," 47th AIAA/ASME/ASCE/AHS/ASC Structures, Structural Dynamics & Materials Conference, Newport, RI, AIAA Paper 2006-20431–4 May 2006.

[7] Masarati, M., Quaranta, G., Ricci, S., and Scotti, A., "Aeroservoelastic Analysis of Morphing Controlled Surfaces," *International Forum on Aeroelasticity and Structural Dynamics*, Stockholm, June 2007.

[8] Bowman, J., Sanders, B., Cannon, B., Kudva, J., Joshi, S., and Weisshaar, T., "Development of Next Generation Morphing Aircraft Structures," 48th AIAA/ASME/ASCE/AHS/ASC Structures, Structural Dynamics, and Materials Conference, AIAA Paper 2007-1730, Honolulu, HI, 23–26 April 2007.

[9] Bye, D. R., and McClure, P. D., "Design of a Morphing Vehicle," 48th AIAA/ASME/ASCE/AHS/ASC Structures, Structural Dynamics, and Materials Conference, AIAA Paper 2007-1728, Honolulu, HI, 23–26 April 2007.

[10] Hetrick, J., Osborn, R., Kota, S., Flick, P., and Paul, D., "Flight Testing of Mission Adaptive Compliant Wing," 48th AIAA/ASME/ASCE/AHS/ASC Structures, Structural Dynamics, and Materials Conference, AIAA Paper 2007-1709, Honolulu, HI, 23–26 April 2007.

[11] Herencia, J. E., Weaver, P. M., and Friswell, M. I., "Morphing Wing Design via Aeroelastic Tailoring," 48th AIAA/ASME/ASCE/AHS/ASC Structures, Structural Dynamics, and Materials Conference, AIAA Paper 2007-2214, Honolulu, HI, 23–26 April 2007.

[12] Siddaramaiah, V. H., Cooper, J. E., Vio, G. A., and Dimitriadis, G., "Drag Minimisation Using Adaptive Aeroelastic Structures," 48th AIAA/ASME/ASCE/AHS/ASC Structures, Structural Dynamics, and Materials Conference, AIAA Paper 2007-1710, Honolulu, HI, 23–26 April 2007.

[13] Vos, R., and De Breuker, R., "Morphing Wing Flight Control Via Postbuckled Precompressed Piezoelectric Actuators," *Journal of Aircraft*, Vol. 44, No. 4, 2007, pp. 1060–1068. doi:10.2514/1.21292

[14] Vos, R., Gurdal, Z., and Abdalla, M., "A Novel Mechanism for Active Wing Warping," 49th AIAA/ASME/ASCE/AHS/ASC Structures, Structural Dynamics, and Materials Conference, AIAA Paper 2008-1879, Schaumburg, IL, 7–10 April 2008.

[15] Diaconu, C. G., Weaver, P. M., and Mattioni, F., "Concepts for Morphing Airfoil Sections Using Bi-Stable Laminated Composite Structures," *Thin-Walled Structures*, Vol. 46, No. 6, 2008, pp. 689–701. doi:10.1016/j.tws.2007.11.002

[16] Kheong, B. L. W., and Jacob, J., "In Flight Aspect Ratio Morphing Using Inflatable Wings," 46th AIAA Aerospace Sciences Meeting and Exhibit, AIAA Paper 2008-425, Reno, NV, 7–10 January 2008.

[17] Seber, G., Sakarya, E., Insuyu, T. E., Sahin, M., Ozgen, S., and Yaman, Y., "Evaluation of a Camber Morphing Concept Based on Controlled Flexibility," *International Forum on Aeroelasticity and Structural Dynamics*, Seattle, WA, June 2009.

[18] Cesnik, C., Last, H. R., and Martin, C. A., "A Framework for Morphing Capability Assessment," 45th AIAA/ASME/ASCE/AHS/ASC Structures, Structural Dynamics & Materials Conference, AIAA Paper 2004-1654, Palm Springs, CA, 19–22 April 2004.

[19] *MSC Patran 2007 r1b, User's Guide*, MSC.Software Corp., Santa Ana, CA, 2007.

[20] *MD Nastran 2006 Implicit Nonlinear (SOL 600) User's Guide*, MSC.Software Corp., Santa Ana, CA, 2006.

[21] "A502 User's Manual: PAN AIR Technology Program for Solving Problems of Potential Flow About Arbitrary Configurations," The Boeing Co., Rept. D6-54703, 1992.

[22] Gern, F. H., Inman, D. J., and Kapania, R. K., "Structural and Aeroelastic Modeling of General Planform Wings with Morphing Airfoils," *AIAA Journal*, Vol. 40, No. 4, 2002, pp. 628–637. doi:10.2514/2.1719

[23] Bae, J., Kyong, N., Seigler, T. M., and Inman, D. J., "Aeroelastic Considerations on Shape Control of an Adaptive Wing," *Journal of Intelligent Material Systems and Structures*, Vol. 16, 2005, pp. 1051–1056. doi:10.1177/1045389X05059965

[24] Phillips, W. F., "Lifting-Line Analysis for Twisted Wings and Washout-Optimized Wings," *Journal of Aircraft*, Vol. 41, No. 1, 2004, pp. 128–136. doi:10.2514/1.262